

# Absolute beam monitor: A novel laboratory device for neutral beam calibration

Cite as: Rev. Sci. Instrum. **93**, 093302 (2022); <https://doi.org/10.1063/5.0092065>

Submitted: 20 March 2022 • Accepted: 10 August 2022 • Published Online: 13 September 2022

 Jonathan Gasser,  André Galli and  Peter Wurz



View Online



Export Citation



CrossMark

## ARTICLES YOU MAY BE INTERESTED IN

[A high-Q superconducting toroidal medium frequency detection system with a capacitively adjustable frequency range > 180 kHz](#)



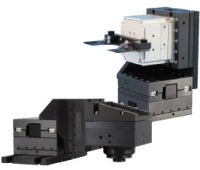
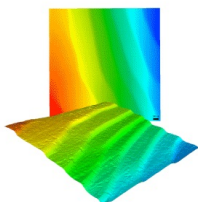
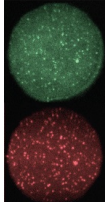
Review of Scientific Instruments **93**, 093303 (2022); <https://doi.org/10.1063/5.0089182>

[Uniformity evaluation of laser-induced periodic surface structures formed by two-color double-pulse femtosecond laser irradiation](#)

Review of Scientific Instruments **93**, 093001 (2022); <https://doi.org/10.1063/5.0096218>

[Characteristic analysis of wideband beam monitor with high-frequency pickups](#)

Review of Scientific Instruments **93**, 093301 (2022); <https://doi.org/10.1063/5.0087321>

 <b>MCL</b> MAD CITY LABS INC. <a href="http://www.madcitylabs.com">www.madcitylabs.com</a>	<p>Nanopositioning Systems</p> 	<p>Modular Motion Control</p> 	<p>AFM and NSOM Instruments</p> 	<p>Single Molecule Microscopes</p> 
---	--	--	---	--



# Absolute beam monitor: A novel laboratory device for neutral beam calibration

Cite as: Rev. Sci. Instrum. 93, 093302 (2022); doi: 10.1063/5.0092065

Submitted: 20 March 2022 • Accepted: 10 August 2022 •

Published Online: 13 September 2022



View Online



Export Citation



CrossMark

Jonathan Gasser,<sup>a)</sup>  André Galli,  and Peter Wurz 

## AFFILIATIONS

Physics Institute, Space Research and Planetary Sciences, University of Bern, Sidlerstrasse 5, 3012 Bern, Switzerland

<sup>a)</sup> Author to whom correspondence should be addressed: [jonathan.gasser@unibe.ch](mailto:jonathan.gasser@unibe.ch)

## ABSTRACT

Instruments recording Energetic Neutral Atoms (ENAs) for space applications require thorough laboratory calibration in a dedicated test facility providing a neutral atom beam. Accurate knowledge of the neutral beam intensity and energy is central for the laboratory calibration procedure. However, until recently, the quantification of the neutral atom beam intensity in the low-energy range below a few 100 eV was based on relative measurements with standard detectors of approximately known detection efficiencies for neutral atoms. We report on the design and development of a novel calibration device dedicated to determining the ENA beam flux in an absolute manner in the energy range from 3 keV down to about 10 eV. This is realized by applying ENA scattering at a surface and coincident detection of scattered particles and created secondary electrons. Moreover, the neutral beam energy is determined by a time-of-flight measurement. The applied measurement principle relies on very low background signals. The observed background count rates are in the range  $10^{-2}$  s for the individual channels and about  $10^{-5}$  s for coincidence events. The background is, thus, at least two, typically four, orders of magnitude lower than the signal rate for neutral atom beams in the foreseen energy range. We demonstrate a concrete application using the absolute flux calibration of a laboratory neutralization stage.

© 2022 Author(s). All article content, except where otherwise noted, is licensed under a Creative Commons Attribution (CC BY) license (<http://creativecommons.org/licenses/by/4.0/>). <https://doi.org/10.1063/5.0092065>

## I. INTRODUCTION

*In situ* and remote detection and analysis of energetic neutral atoms (ENAs) has become an important method in space and planetary science.<sup>1</sup> Several past and upcoming space missions are equipped with a low-energy ENA imaging instrument, such as IBEX-Lo<sup>2,3</sup> on the very successful and still active Interstellar Boundary Explorer (IBEX) mission by NASA<sup>4</sup> and its successor Interstellar Mapping and Acceleration Probe (IMAP),<sup>5</sup> with launch scheduled for February 2025. The scientific instruments onboard these spacecraft are dedicated to investigate in great detail the heliosphere and its interaction with the Local Interstellar Medium. IBEX provided many new insights into the structure and physical processes of the outer heliosphere, in particular, the discovery of the ENA ribbon and characterization of the globally distributed ENA flux. Annual all-sky ENA maps and interstellar neutral atom observations have been acquired over one full solar cycle,<sup>6</sup> and references therein.<sup>7–9</sup> The active science phase of IBEX is expected to continue until 2025, allowing for overlap between the IBEX and IMAP

missions. Cross-calibration measurements will be performed in flight between IBEX-Lo and IMAP-Lo, once the latter begins science operations.

ENA observations are particularly interesting in heliospheric science because neutral atoms, as opposed to electrons and ions, travel on ballistic trajectories and are not affected by solar wind plasma and magnetic fields. They, thus, provide a pristine source of information about conditions present at their origin, such as density, composition, bulk speed, and energy distribution of the Local Interstellar Medium. In addition, ENA instruments also allow for the remote sensing of planetary atmospheres.

ENA instruments for planetary exploration include IMAGE/LENA,<sup>10</sup> ASPERA-3 on Mars Express<sup>11</sup> and ASPERA-4 on Venus Express,<sup>12</sup> CENA/SARA<sup>13</sup> on the lunar mission Chandrayaan-1, SERENA/ELENA and ENA as part of the Mercury Plasma/Particle Experiment on BepiColombo<sup>14,15</sup> launched in October 2018 heading for Mercury, Mars Ion and Neutral Particle Analyzer (MINPA)<sup>16</sup> on the Chinese Mars mission (Tianwen-1), and the Jovian Neutral Analyser (JNA)<sup>17,18</sup> as part of the Particle

Environment Package on the upcoming JUICE (Jupiter Icy Moons Explorer) mission<sup>19</sup> to be launched in 2023.

Low-energy ENA instruments below a few 100 eV generally rely on an efficient and reliable particle ionization method to allow for electrostatic analysis and post-acceleration in support of detection efficiency.<sup>1</sup> The most widely used technique for space applications in this energy range is charge-conversion via on-surface scattering at grazing incidence angles.<sup>1</sup> However, the underlying physical processes involved in the atom-surface interactions are not yet understood in full detail. Instead, a number of well-suited conversion surface materials have been characterized experimentally,<sup>20</sup> and references therein.<sup>21,22</sup>

For this reason, besides the general specification necessities imposed by the harsh space environment, ENA detection instruments require proper calibration against a neutral atom beam source. For full instrument calibration, substituting the ENA beam by an ion beam is not feasible because low-energy ions, as opposed to neutral atoms, are affected by electric fields inside the instrument under test.

At the University of Bern, we have a dedicated laboratory test facility<sup>23</sup> available for preflight calibration of ENA instruments for space research. The MEFISTO facility is equipped with an electron cyclotron resonance ion source (ECRIS) suitable for producing a positive ion beam from any atomic species. Calibration of the IMAP-Lo instrument will be carried out there. For the IMAP-Lo calibration campaign, calibrated ENA beams from hydrogen, oxygen, helium, and also deuterium, neon, and other light elements are of foremost interest.

In the low-energy range, a neutral beam is obtained from a collimated ion beam via surface neutralization using the neutralizer.<sup>24</sup> This neutralization process introduces angular divergence and some kinetic energy loss upon scattering from the neutralization surface. After beam neutralization in the laboratory, beam characterization by means of particle detection devices such as multichannel-plate detectors and channeltrons is limited by the knowledge of the absolute detection efficiency of these detection devices for atoms at these energies. Until recently, energy loss and neutral beam intensity were estimated based on relative measurements and theoretical considerations, as it was not possible to experimentally determine neutral beam fluxes and energies directly.<sup>24</sup>

The rising demand for an accurate method to determine the ENA flux of a neutral atom beam source urged us to develop the Absolute Beam Monitor (ABM), in particular, in regard of the upcoming IMAP-Lo calibration campaigns. The ABM is a laboratory device used to determine the particle flux of a neutral atom beam in the energy range from 3 keV down to 10 eV. Using coincidence events in this device allows for absolute flux measurements in a manner independent of any implicit detection efficiency assumption. It will, therefore, be used as primary standard for the laboratory ENA beam source calibration. The ABM is so far the only device to measure absolute neutral beam intensities in the energy range below 1 keV.

The general approach for measuring the absolute flux of neutral atom beams using coincidence events has already been used.<sup>25</sup> This instrument uses the neutral beam transmission through a thin foil. Given that the atoms have to pass solid matter, a thin foil, there exists a minimum value of energy the atoms need to possess for their registration. This minimum energy given by the successful

transmission through the foil is around 500–1000 eV/nuc,<sup>1,26</sup> increasing with foil thickness. The energy threshold for H detection using thin carbon foils of 1  $\mu\text{g}/\text{cm}^2$  is about 500 eV, and it increases with atomic mass  $m$ ; as for fixed energy, the nuclear stopping in the foil is approximately proportional to  $m^{27}$  and the angular scatter increases with the mass as well.<sup>28</sup> For IMAP-Lo, the required mass range spans from 1 to 32 (hydrogen to sulfur) in the energy range from 10 eV to 2 keV; thus, the foil-based approach cannot be used.

## II. METHODS

In the following, we describe the ABM design and implementation as well as the basic physical principle it is built on.

### A. Measurement principle

The detection and analysis of low-energy ENAs require prior particle ionization. The most reliable ionization process used in space science at energies below about 1 keV is via on-surface interaction at grazing incidence angles.<sup>29</sup> The grazing incidence surface scattering process is also applied to obtain an ENA beam from a primary ion beam.<sup>24</sup> In the scattering interaction, secondary electrons are ejected from the surface, which can be detected separately.

The ABM measurement principle relies on coincident detection of a neutral atom scattered off a conversion surface and the simultaneous release of a secondary electron during this scattering process. The absolute neutral atom flux  $f_n$  entering the ABM is determined by the number of counts  $N$  for the detected neutral atoms within a time interval  $t_{\text{int}}$ , the detection efficiency  $\epsilon_n$  for neutral atoms, and the cross section  $\sigma_{ap}$  of the ABM aperture,

$$f_n = \frac{N}{\epsilon_n \sigma_{ap} t_{\text{int}}} = \frac{n}{\epsilon_n \sigma_{ap}}. \quad (1)$$

The measured neutral atom rate,  $n$ , is obtained by the simultaneous detection of three count rates: a start count rate  $r_e$  generated by secondary electrons released from the start surface (SS) upon impact of a neutral atom, a stop count rate  $r_i$  of the scattered neutral atoms hitting the stop detector, and a coincidence rate  $r_c$  between these two signals. Each incident neutral atom has an *a priori* unknown probability  $\eta_e$  for ejecting a secondary electron from the SS and an unknown probability  $\eta_i$  of being itself detected subsequently by the stop detector. The probability of generating a coincidence count is, thus,  $\eta_c = \eta_e \cdot \eta_i$ . The start, stop, and coincidence count rates ( $r_e, r_i, r_c$ ) to be observed from the incoming neutral atoms  $F_n = f_n \sigma_{ap}$ , through the entrance aperture with the cross section  $\sigma_{ap}$ , respectively, will then be

$$\begin{aligned} r_e &= \mu_e F_n + r_{e,0}, \\ r_i &= \mu_i F_n + r_{i,0}, \\ r_c &= \mu_c F_n + r_{c,0} = \mu_e \mu_i F_n + r_{c,0}. \end{aligned} \quad (2)$$

With the requirement that the backgrounds on the three rates ( $r_{e,0}, r_{i,0}, r_{c,0}$ ) are negligible, we obtain

$$\begin{aligned}\mu_e &= \frac{r_c}{r_i} = \frac{\mu_e \mu_i F_n}{\mu_i F_n}, \\ \mu_i &= \frac{r_c}{r_e} = \frac{\mu_e \mu_i F_n}{\mu_e F_n},\end{aligned}\quad (3)$$

and we get the detection efficiency  $\varepsilon_n = \mu_e \mu_i$ , for neutral atoms. This formalism is well known and has been used in plasma and particle instruments for many years.<sup>30,31</sup> The neutral atom flux  $f_n$  can be obtained directly from the observed count rates as

$$f_n = \frac{(r_e - r_{e,0}) \cdot (r_i - r_{i,0})}{(r_c - r_{c,0})}. \quad (4)$$

This method requires very low detector background count rates; otherwise, the background rate in the start rate  $r_{e,0}$ , the stop rate  $r_{i,0}$ , and the coincidence rate  $r_{c,0}$  will interfere with the derivation of the neutral atom flux. Therefore, we have to keep the background rates very low compared to the respective count rates to apply Eq. (4) to derive the true particle flux  $f_n$ . We carefully record the background count rates separately, see below, and subtract them from the measured count rates in the data evaluation.

By multiplying the rates with the integration time, we can rewrite Eq. (4) by the actual counts collected:

$$f_n = \frac{(c_e + c_{e,0}) \cdot (c_i + c_{i,0})}{(c_c + c_{c,0})}. \quad (5)$$

We assume that the individual counts registered in a time interval are Poisson distributed. The statistical uncertainty of the mean count rate for a single accumulation measurement is, thus,

$$\frac{\delta f_n}{f_n} = \frac{\delta c_e}{c_e} + \frac{\delta c_i}{c_i} + \frac{\delta c_c}{c_c} = \frac{1}{\sqrt{c_e}} + \frac{1}{\sqrt{c_i}} + \frac{1}{\sqrt{c_c}}. \quad (6)$$

The dominant contribution to the statistical uncertainty is due to coincidence counts, as these always give the lowest count rates. At lower beam energies, where the neutral atom flux is typically much reduced, this puts a condition on the required accumulation time: To achieve a relative uncertainty of 10% or better in Eq. (6), the integration time should be long enough to record at least 100 coincidence counts.

From all recorded coincidence events, we measure the time difference  $\Delta t$  between the start pulse and the stop pulse in parallel to the individual counters. Combined with the known mean flight distance  $s$  of scattered atoms from the SS center to the stop detector and the atom species (known from the primary ion beam), we infer the kinetic energy as

$$E_{kin} = \frac{m_0}{2} \langle s \rangle^2 (t_{el} + \Delta t)^{-2}. \quad (7)$$

Here, we also take into account the electron flight time  $t_{el}$  from the SS to the start detector, which is about 11 ns according to the electro-optical simulation.

Neutral atoms can impinge over almost the full length of the SS, which causes an uncertainty  $\delta s$  in the flight distance after generating a start signal. With  $\langle s \rangle = 101$  mm and  $\delta s = \pm 10$  mm, this contributes a relative uncertainty of  $\frac{\delta E}{E} \cong 10\%$  to the energy distribution measured in the time-of-flight (ToF) spectra.

## B. Technical design

The ion-optical properties and the geometry were designed using numerical simulations with the SIMION® software package from Scientific Instrument Services. A schematic overview of the simulation model is shown in Fig. 1.

The ABM consists of a near-cylindrically shaped box of about  $14 \times 7 \times 7$  cm<sup>3</sup> size. The structure is an assembly of a concave top plate and an opposite bottom plate with a conical rim, enveloped by a cylindrical mantle with flattened planar sides. A circular entrance hole of 5 mm diameter is located at the front side of the envelope, the entrance aperture, through which the ENAs enter the ABM. An additional circular aperture of 5 mm diameter is mounted 9 mm in front of the entrance aperture to restrict the allowed angular directions of incoming neutral atoms. At the backside, a passage in the mantle is left open and a conical tube (target cone) is firmly attached. Serrations in the bottom plate and target cone serve to collect the scattered particles off the SS. All inner surfaces, except for the SS and the channel electron multipliers (CEMs), are coated with Acktar Vacuum Black (Acktar Ltd., Kiryat-Gat, Israel) to enhance absorption of photons, electrons, and scattered atoms by its large effective surface area.

The whole ABM is tilted by about 10° with respect to the neutral beam direction, so that the ENA beam entering through the entrance aperture hits the SS at a grazing incidence angle of  $\alpha = 10^\circ \pm 0.5^\circ$ . This shallow incidence angle is a compromise between reducing the angular scattering on the SS by a more grazing incidence on one hand and capturing the full incident ENA beam on a relatively short SS not to broaden the ToF peak on the other hand. Moreover, the same incidence angle was applied in the surface neutralizer (see below). The SS stands off from the top plate and is oriented along the projected neutral beam direction to cover the full neutral beam passing through the entrance hole.

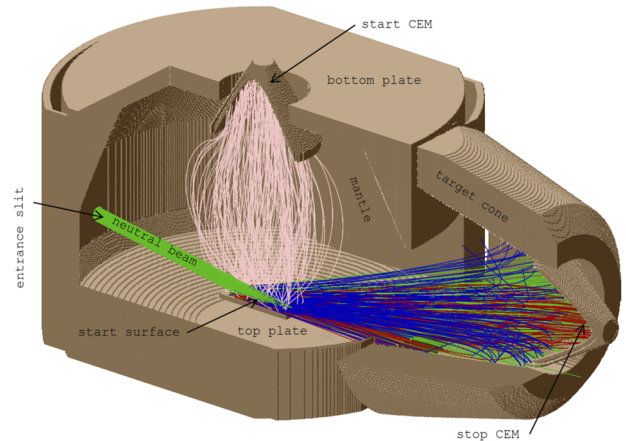


**FIG. 1.** Schematic ABM simulation model in SIMION. Part of the structure is cut away to present the ABM interior. Simulated particle trajectories are shown as colored lines: neutral atoms (green), electrons (pink), positive ions (red), and negative ions (blue) ions. The ABM device is operated such that the neutral atoms enter horizontally through the entrance aperture on the left.

A first channel electron multiplier (start CEM) of 25 mm diameter is placed opposite the SS. Its entrance is held at a positive electrostatic potential (HV0) to attract all secondary electrons emitted from the SS. A second CEM (stop CEM) is placed at the open end of the target cone to accept and detect the scattered neutral atoms.

The entire enclosure (mantle, top and bottom plates, target cone) is at ground potential. The SS at a low positive voltage and the start CEM at +HV0 confine the secondary electrons in the center region of the volume. Scattered charge-converted ions and neutral atoms are directed, simply by their scattering direction distribution, toward the stop CEM with aperture at a high negative potential (HV2). Negative ions are, thus, rejected and effectively absorbed at the inner device walls, while positive ions are attracted toward the stop CEM.

The start surface is, of course, the central element of the entire device. It consists of a  $20 \times 10 \times 1.0 \text{ mm}^3$  highly polished tungsten (W) single crystal plate (MaTeck GmbH, Jülich, Germany) with (100) surface orientation. Tungsten was chosen as SS to have the same surface interaction as in the neutralizer, to support the validity of Eq. (10) (see below) for the relative loss of particle energy. In the neutralizer design,<sup>24</sup> W was used as neutralizing surface for three reasons: First, metal single crystals serve well to neutralize scattered particles; second, W isotopes have high atomic masses of 182–186 amu, which aids in reducing the energy transfer in a binary collision with low-mass atomic ions;<sup>20,32</sup> and third, W single crystal surfaces are readily available and chemically stable. The SS plate is soldered at its backside onto a screw, which is fed through the top plate but electrically insulated from it. A bias low voltage is applied on the mounting screw from the outside. The SS is equipped with an electrically insulated resistive wire heater at its backside that allows heating the SS to remove adsorbed water layers from it.

The start CEM aperture cone is inserted through a circular hole in the bottom plate; its electrical connections and signal line are placed under the box. Two semicircular inserts close up the hole for electrostatic shielding. The stop CEM holder is mounted at the back of the target cone. The entire device is mounted on a  $10^\circ$  tilted aluminum support that ensures proper geometry for the incidence of the neutral atom beam, proper electrical ground, and firm and flexible installation in the vacuum chamber. Figure 2 shows a photograph of the assembled ABM device.

### C. Laboratory setup

The ABM has been tested and mounted in the MEFISTO test facility.<sup>23</sup> MEFISTO consists of a large vacuum chamber equipped with a microwave-heated electron cyclotron resonance ion source providing a focused positive ion beam of any desired species at energy 3 keV/q. The ion beam is neutralized using the surface neutralizer, which has been moved into the ion beam path.<sup>24</sup> Inside the neutralizer, the incoming ions are scattered at a  $10^\circ$  grazing incidence angle from a polished W surface and, thereby, almost completely neutralized. The neutralizer can be floated to high voltage up to 3 kV, which decelerates the incoming ion beam to the desired final ion energy in the range 10–3000 eV for neutralization. A  $20^\circ$  electrostatic analyzer, with ions of defined energy, is installed in front of the neutralization surface to deflect the ion beam so that

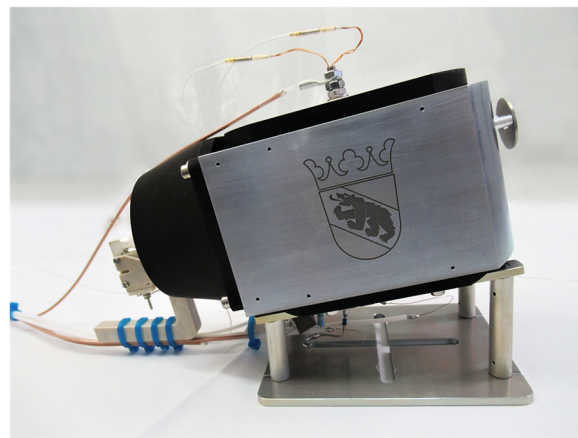


**FIG. 2.** The fully assembled absolute beam monitor version 2. The entrance aperture with the additional standoff aperture is to the right. At the top is the SS mounting screw with the SS voltage connection and the heater connections. Electrical connections for the CEMs come from the left underneath the ABM. The dimension of the base plate is  $100 \times 80 \text{ mm}^2$ .

the outgoing neutral beam is parallel to the incoming ion beam. The neutralization process induces an estimated 15% reduction in beam energy and the deceleration induces an energy-dependent transmission. The neutral beam flux into the test chamber, thus, varies with ion beam energy, ion intensity, and species.

During testing, the ABM is mounted on a four-axis movable and pivotable hexapod table so that the ABM can be placed in the optimal position at the center of the neutral beam in front of the neutralizer exit at a distance of about 10 cm (see Fig. 3). The entire test setup incorporates, thus, a collinear and retarded ion beam passing through an ESA onto a neutralizing W surface. The resulting

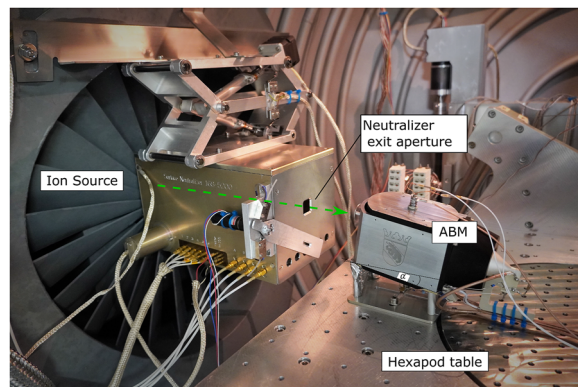


**FIG. 3.** The ABM mounted on the hexapod table in the MEFISTO vacuum chamber, placed at the exit of the surface neutralizer. At the front, toward the neutralizer, there is the entrance aperture and the aluminum shielding to protect the start CEM under the ABM box. The ion beam enters the neutralizer from behind the baffled shroud on the left-hand side. The neutral beam axis (green) and ABM tilt angle are indicated. Scale: The screw hole spacing on the hexapod table is  $40 \times 40 \text{ mm}^2$ .

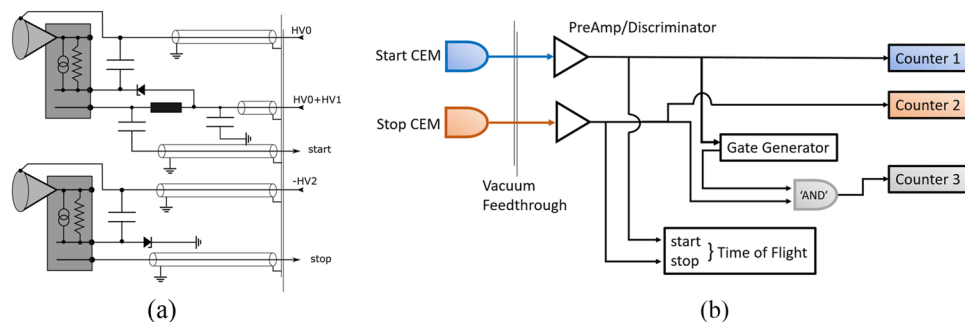


**FIG. 4.** (a) Electronic circuitry of the start (top) and stop CEM (bottom). Gray boxes represent the CEMs with electrical front, back, and anode contacts. The CEM apertures are held at high voltage +HV0 and −HV2, respectively. (b) Electronic signal processing setup in the laboratory. The preamplifiers transform the negative signal pulses from the CEMs to clean rectangular positive pulses. The gate generator provides the time window for coincidence events. ToF spectrum acquisition is done using a separate TDC card.

neutral atom beam is collimated at the neutralizer exit and passes on into the ABM where the neutral atoms strike another W surface to initiate detection.

Secondary electrons or scattered ions and neutral atoms from the ABM SS are collected in the CEMs (Sjuts Optotechnik GmbH, Germany, model KBL25RS/90) with 25 mm diameter apertures. The negative signal pulses from the start and stop CEM are routed through the vacuum chamber flange and fed into a preamplifier and discriminator (Winkelnkemper Ing., Hattingen, Germany, model PAD06DS), which converts the CEM signals into 12 ns short +1.5 V rectangular pulses for further processing. The preamp dead time was set to 20 ns. The electronic configuration is shown in Fig. 4.

The discrete start pulses are recorded by the electronic Counter 1 (model: HP 53132A), as shown in Fig. 4(b). The signal also triggers the gate generator (model: Stanford DG535) that outputs a coincidence window signal of adjustable duration. The discrete stop pulses are registered alike in Counter 2 (model: Keithley 776) and in Counter 3 (model: Keithley 775A) during active gate window signal to accumulate the coincidence counts. A signal delay through the gate generator is matched by accordingly longer stop signal line. Compared to a conventional coincidence counting system, the expected flight time of a particle covers a large range; thus, we allow for a long coincidence gate window in the range 100 ns to 10  $\mu$ s, depending on species and beam energy. For each start event, several stop counts could be accepted as coincidence events.

In addition, the time intervals between start and stop pulses for coincidence events were recorded using a fast time-to-digital converter (TDC) card (FAST ComTec GmbH, Oberhaching, Germany, model p7886) with up to 2 GHz (0.5 ns) time resolution. The hardware is installed directly on the main board and operated with commercial software. The TDC acquisition features an end-of-sweep dead time of about 20 ns. All start and stop signal lines and counter and preamplifier thresholds were matched to ensure a maximal shift of <0.1 ns in time difference owing to the setup.

### III. PERFORMANCE CHARACTERIZATION

Several tests were undertaken in support of performance and concept verification.

### A. Background rates

The background count rate refers to the number of detected signal pulses per time with the beam source and surface neutralizer shut down but the ABM fully working. Background counts may result from ambient ions or electrons from the pressure gauges hitting one of the CEMs or from spontaneous pulses from radioactive decay of materials used in the CEMs. Moreover, electronic noise may be picked up on the signal transmission lines. The ambient gas pressure in the test chamber was in the low to mid  $10^{-8}$  mbar range. In Fig. 5, the measured background count rates are displayed over time. These were usually acquired over several hours. The start background rate is in the order of 1 min, the stop background rate is about 0.3 min, and the coincidence background rate is typically below 0.001 min (i.e., below  $10^{-5}$  s $^{-1}$ ). The exponential fits to the data provided in Fig. 5 show a decrease in background counts over time for the start and stop signals, whereas the coincidence background count rate remains constant over time within the uncertainties given due to the very low counting statistics.

For the most part of the foreseen energy range, the background count rate of each channel is at least two orders below the measured actual signal count rate. Only for the very low-energy neutral atom beams (below about 50 eV), it might become relevant to subtract the background count rate for proper data evaluation.

### B. Poisson distribution

The detection of individual secondary electrons is independent, but for a constant neutral atom beam flux, the detection probability is constant in time. Likewise, for the detection of scattered atoms. Therefore, the number of detected start or stop counts  $n$  per unit time interval  $\Delta t$  should follow a Poisson distribution with expectation value  $\langle N \rangle$ ,

$$p(n, \Delta t) = \frac{\langle N \rangle^n}{n!} e^{-\langle N \rangle}. \quad (8)$$

This can best be tested in a measurement at low beam energies, where the mean start or stop count rates are just a few counts per time interval, i.e., typically about 5 counts/min. A constant ion beam intensity is required to establish time independence of the detection probability. Figure 6(a) shows start and stop counts over time of a measurement sequence with a 50 eV hydrogen neutral atom beam having low count rates, and Fig. 6(b) shows the histogram for a

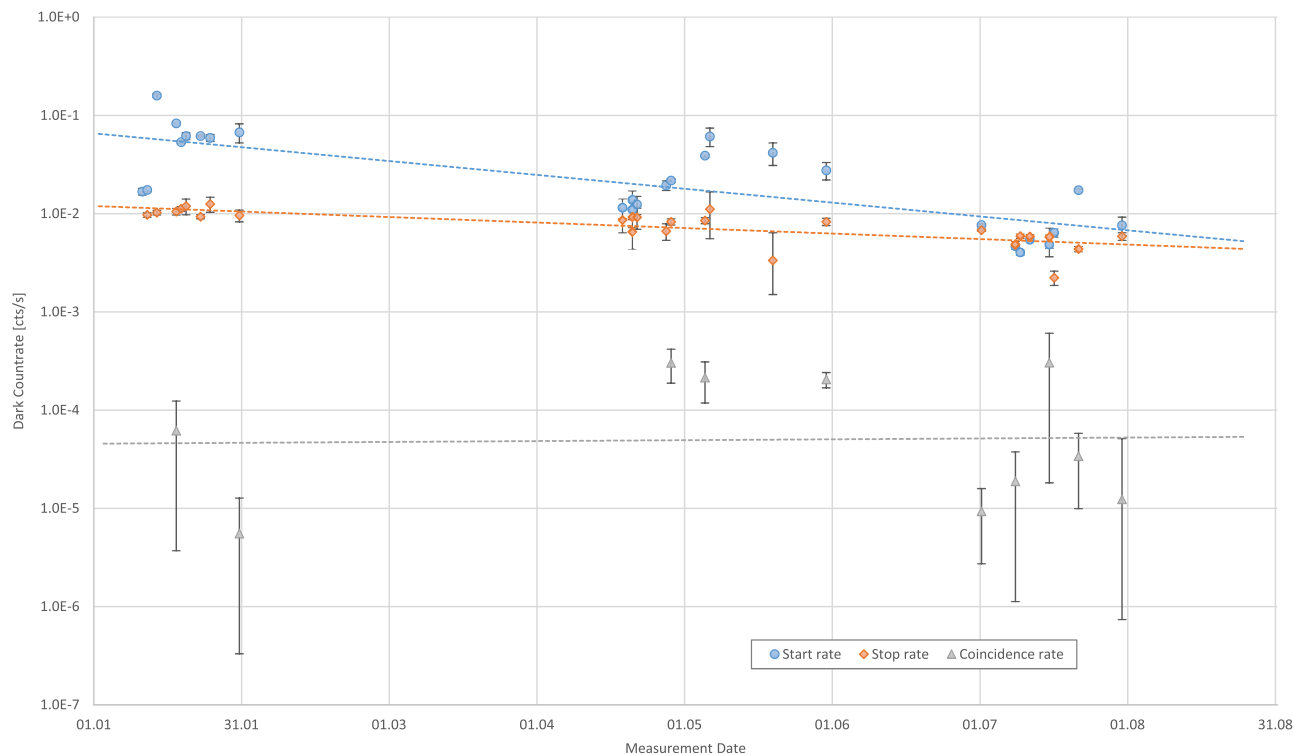


**FIG. 5.** Measured ABM background count rates for start, stop, and coincidence over time shown with statistical errors. The typical acquisition time per data point is several hours. Zero coincidence background counts were recorded where the respective data points are missing. Weighted exponential fit curves are added for each channel.

60 s time interval of these counts along with the Poisson distribution corresponding to the mean count rate. Figure 6(c) shows the respective start, stop, and coincidence count distributions at a beam energy of 80 eV giving higher count rates. The measured distributions are in good agreement with Poisson distributions, confirming that individual atoms or secondary electrons are indeed recorded independently.

This holds true as long as the mean start or stop count rate is small compared to the inverse of the preamplifier dead time,  $n \ll \tau_d^{-1} \equiv (10 \text{ ns})^{-1} = 10^8 \text{ s}^{-1}$ . At the highest ENA energies, where we encounter the highest count rates, the start count rate remained below  $10^7 \text{ s}^{-1}$ , most times below  $10^6 \text{ s}^{-1}$ .

### C. Background and voltage setting

A typical measurement sequence of a neutral hydrogen atom beam at an ion energy of 100 eV/q, during optimization of the measurement parameters, is shown in Fig. 7. Counts were collected for 60 s accumulation time and these data points were stored continuously. The total measurement time is close to 5 h. The number of measured neutral atoms per time unit is calculated from the respective start, stop, and coincidence counts. Several manipulations were done on the CEM voltages (HV1, HV2) and the offset voltage (HV0) during this sequence to optimize the operation of the ABM. Times of these changes are indicated by dashed lines in Fig. 7, with the details given in Table I.

These adjustments on the CEM voltages have a large impact on the start, stop, and coincidence count rates. In particular, increasing the start CEM voltage HV1 by 150 V in total from minute 1 to minute 120 increases the start count rate by about three orders of magnitude until a plateau is reached and similarly for the coincidence events. However, the deduced neutral atom rate is only lower by a factor 3 before compared to after minute 90, when the HV1 voltage reached the nominal level. The large scatter in intensity of neutral atoms during the first hour is a direct consequence of the extremely low start rate and, thus, the extremely low coincidence rate. Increasing HV1 further (around minute 240) leaves the obtained neutral atom rate constant. Furthermore, adjusting the offset voltage HV0 within a range of a few 100 V (after minute 240) does not affect the resulting neutral atom rate despite changes in the individual count rates. Consequently, the offset voltage can be used to minimize the relative statistical variation of the neutral atom rate, by maximizing the coincidence count rate. In summary, once a sufficiently high voltage is applied to the CEMs, their actual value is less critical, and a stable and reliable neutral flux can be derived from these measurements. Changing the preamplifier threshold voltages (minutes 44, 120, 210) does in general also affect the individual start, stop, and coincidence count rates but not the derived neutrals rate.

At minutes 105, 175, and 218, the primary hydrogen ion beam was blocked intentionally by the ion beam scanner for several minutes. This reduced the start and stop counts by four orders of

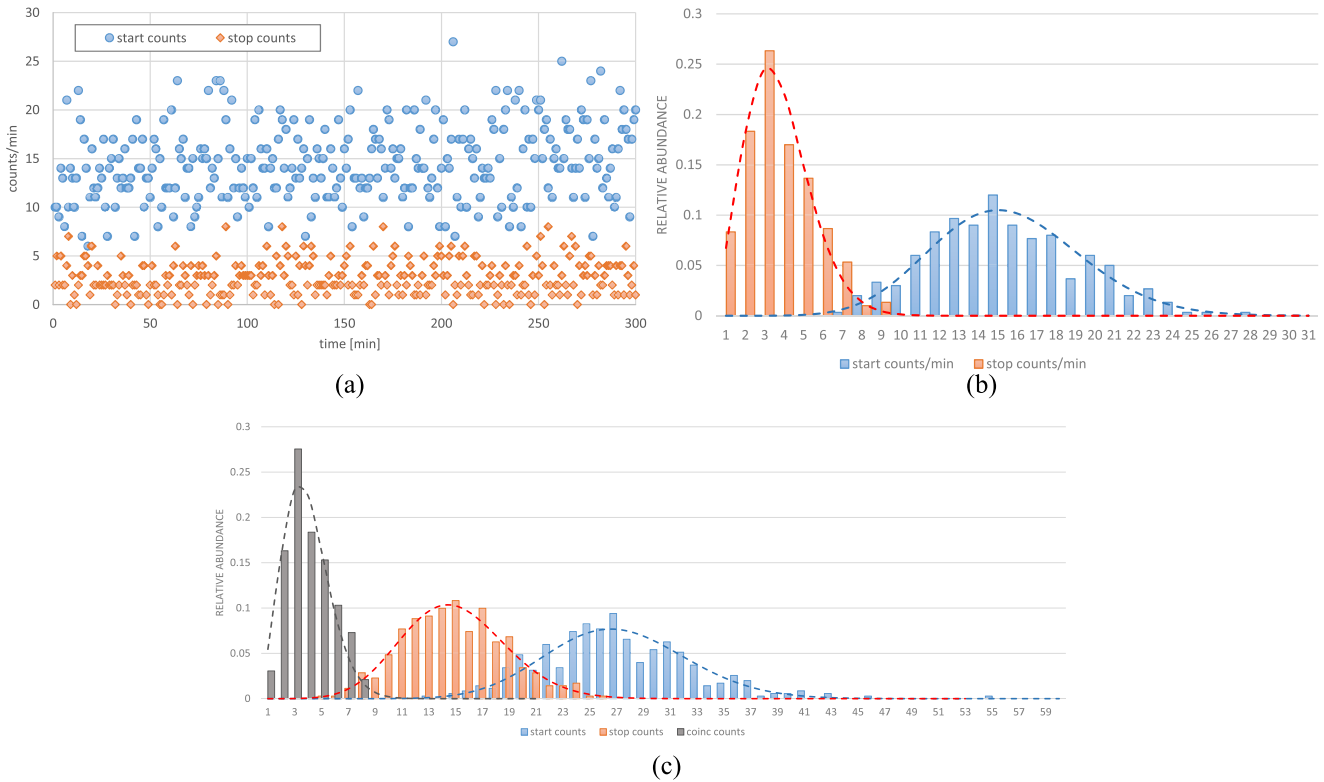


**FIG. 6.** (a) Example time sequence of start and stop counts for H at 50 eV. (b) Corresponding occurrence distribution (histograms) and predicted Poisson distributions (dashed lines). Expectation values are  $\langle N \rangle = 14.5$  and  $\langle N \rangle = 2.7$  for start and stop counts, respectively. (c) Start, stop, and coincidence distributions at slightly higher count rate for 80 eV hydrogen. The dashed lines show predicted Poisson distributions for  $\langle N \rangle = 2.91$ , 14.9, and 27.07 counts/min, respectively.

magnitude to their respective background rates, giving a signal to background ratio of about  $10^4$  for the start rate, as well as for the stop rate. The mean start and stop count rates are indicated, respectively, for each ion beam interrupt period by empty symbols with statistical error bars. No coincidence events were detected during the ion beam interrupts, which is expected given the low coincidence background rate of about  $10^{-4} \text{ s}^{-1}$  presented in Fig. 5. The ion beam interruptions demonstrate the low background during a real measurement situation, in agreement with the background determinations done during the preparation (Fig. 5), which are a requirement for the capability of absolute neutral flux measurements with the ABM.

#### D. Time-of-flight measurement

The TDC card used for the ToF measurements provides time resolution of up to 0.5 ns. The data acquisition speed is, thus, considerably higher than the physical ToF resolution of the ABM, and we obtain a well-resolved peak in the ToF spectra given large enough coincidence events statistics. Acquisition of ToF spectra of variable length (512 ... 8192 bins) and bin size ( $2^{x-1}$  ns,  $x \in \mathbb{N}$ ) can be adjusted to neutral beam species (H, O, He) and estimated energy.

The recorded ToF spectra are subsequently transformed into kinetic energy spectra according to Eq. (7) and need be rescaled by

the factor to compensate for the varying bin width in the energy spectrum,

$$n(E) = \frac{dt}{dE} \cdot n(t) = \frac{\langle s \rangle}{2} \sqrt{\frac{m_0}{2E^3}} n(t), \quad (9)$$

where  $\langle s \rangle$  is the mean flight distance and  $t$  the individual flight time. Any constant background contribution in the ToF spectrum transforms into a power-law background proportional to  $E^{-3/2}$ . We subtract this background, if present, by fitting the nonpeak domain in the energy spectrum by the mentioned power law to obtain the cleaned energy peak.

Note that in this setup, the detected ENA undergoes two surface scattering interactions from the ion beam entering the neutralizer to the ABM's stop CEM, first at the beam-neutralizing surface, then in the ABM. We take advantage of the fact that the SS in the ABM and in the neutralizer are highly polished single crystal W surfaces at  $10^\circ$  incidence angle each. Thus, the relative energy loss will be roughly the same, and we obtain the relative energy loss in each surface interaction as

$$\frac{\Delta E_{NS}}{E_{ion}} = \left( 1 - \sqrt{\frac{\langle E \rangle_{tof}}{E_{ion}}} \right). \quad (10)$$



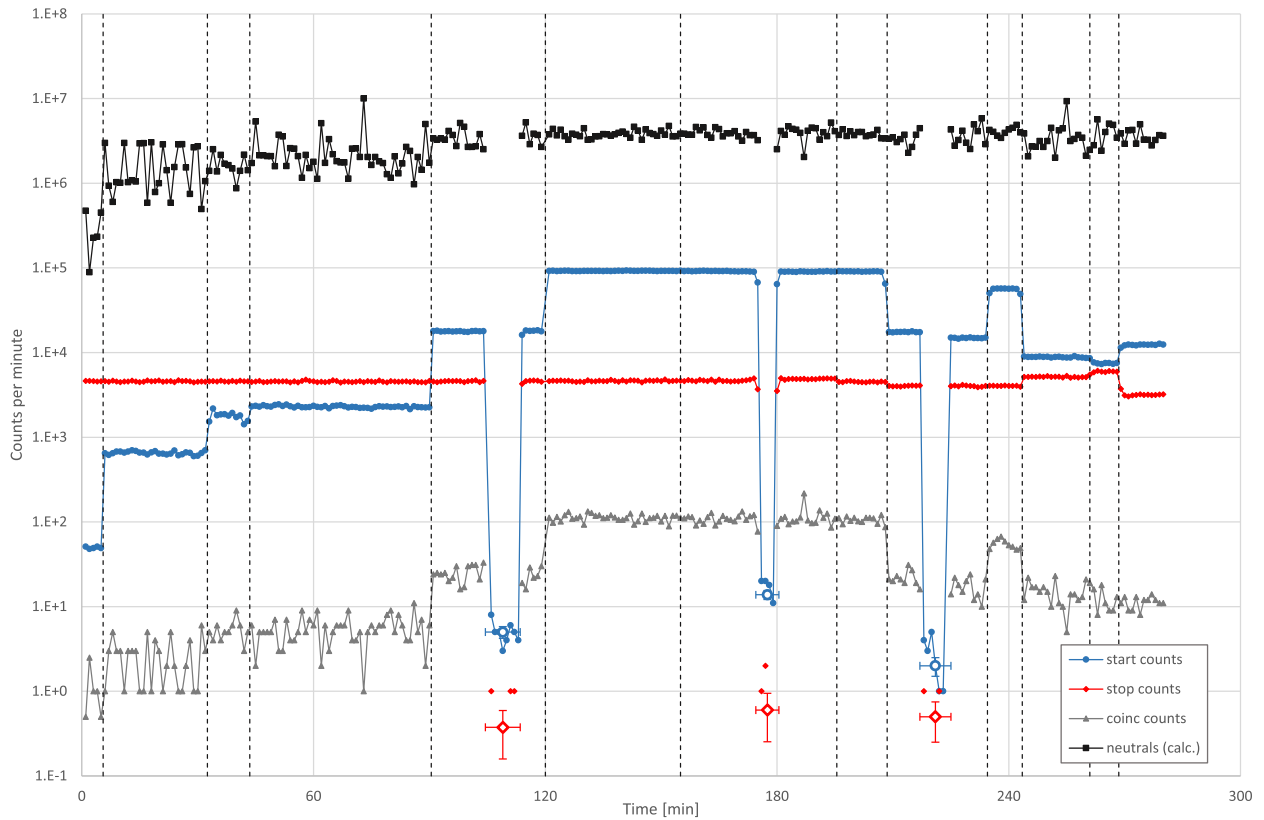


**FIG. 7.** Example measurement sequence with a 100 eV neutral hydrogen beam. The total measurement time is 280 min. Vertical dashed lines represent times of manipulations on the voltage configuration. At minutes 105, 175, and 218, the hydrogen beam was blocked for several minutes.

**TABLE I.** Sequence of the voltage setting during the measurement campaign presented in Fig. 7, taken with the ABM on 5 July 2021.

Minute	Changes
00	HV1 = 2.25 kV, HV2 = -2.35 kV, HV0 = 600 V, $\Delta t_{coinc} = 2.0 \mu s$
06	HV1 = 2.31 kV
33	HV1 = 2.36 kV
44	HV1 = 2.41 kV, adjust the start preAmp threshold to higher level
90	HV1 = 2.45 kV
105–113	Ion beam interrupted by ion beam scanner (Faraday cup)
120	Start preAmp threshold adjust to lower level (as was at start)
155	Shorter gate window: $\Delta t_{coinc} = 1.5 \mu s$
170	Stop preAmp threshold adjust to lower level
175–180	Ion beam interrupted by Faraday cup
195	Reduced stop CEM voltage: HV2 = -2.30 kV
210	Altered both preAmp thresholds
218–225	Ion beam interrupted by Faraday cup
235	HV1 = 2.49 kV (increased)
244	HV1 = 2.45 kV, HV0 = 500 V (lowered)
261	HV0 = 430 V (lowered)
270	HV0 = 700 V (increased)

The ion beam energy is obtained directly from the difference between neutralizer float voltage and ion-source post-acceleration voltage and from the neutralizer ESA voltage.

Figure 8(a) shows an example ToF spectrum of hydrogen and Fig. 8(b) the resulting energy spectrum. The energy peak is fitted with a Gaussian, and the mean energy ( $E$ ), the peak width, and standard error are read out. The energy peak width is a convolution of several contributions: the variation in flight distance  $\delta s$  from different scattering locations on the SS mentioned earlier and impinging points on the stop CEM funnel, an estimated  $\pm 2$  ns variation in start electron flight time to produce start signals, the energy spread resulting from scattering from the SS, and the actual energy spread in the neutral atom beam.

As the stop CEM is at negative high voltage, positive ions scattered off the SS are accelerated toward the stop CEM and, thus, show a lower ToF than the neutral atoms. At high energies, ions provide only a minor contribution to the ToF peak and cannot be separated from the neutral peak: The ToF difference between ions and neutral atoms in the ABM is smaller than the peak width. At low energies, ions have a considerably lower ToF than the neutral atoms and may make up a larger fraction of the stop signals due to their higher detection efficiency. Having sufficient statistics, one can separate the peaks of ions and neutral atoms. In this case, only the neutral peak has been used for ToF evaluation. At intermediate energies, where the contribution of ions to the ToF peak is not negligible and cannot be uniquely separated, this may introduce some systematic uncertainty in broadening the ToF peak.

With higher atomic mass and/or lower beam energy, the peak in ToF spectrum shifts to larger flight time. By comparison of the ABM measured mean energy of neutral atoms to the primary ion energy, the energy loss during the scattering interaction with a tungsten surface is inferred. From the spectrum shown in Fig. 8, we get a mean energy of  $\langle E \rangle = 862$  eV and a peak FWHM of 533 eV. Relating this mean energy to the primary ion beam energy of 1300 eV

using Eq. (10), we obtain a mean energy loss per surface interaction of about 18% in this case.

### E. Neutral atom beam calibration

As described above, until recently, the ENA flux from the surface neutralizer in the energy range of 10 eV–1 keV had to rely on the known detection efficiency for neutral atoms of the used detector, which was an MCP-based imaging detector, and allowed for a calibration with neutral atoms with 30% accuracy.<sup>2</sup> This detection efficiency was derived in earlier work on MCP detectors in a different laboratory.<sup>33</sup> One key purpose of the ABM is to determine the incoming neutral atom rate independent of the prior knowledge of the detection efficiencies of the detector using the described start–stop–coincidence method. Combined with the well-defined entrance aperture, it amounts to determining the ENA beam flux  $f_n$  (part  $\text{cm}^{-2} \text{s}^{-1}$ ) as a function of primary ion beam energy  $E_q$ . In the neutralizer, the current on the neutralizer surface  $I_{ncs}$  from the impinging positive ions is measured. This current mostly reflects the primary ion current, with contributions from secondary electron emission by the ion impact, and a small fraction of scattered negative ions. The  $I_{ncs}$  is permanently recorded during the neutralizer operation with a highly sensitive pico-amperemeter.

The ENA flux generated in the neutralizer from an ion beam at a given species and beam energy is proportional to the measured current at the neutralizer surface,<sup>24</sup> which is proportional to the ion flux hitting the tungsten surface. The proportionality is a combination of neutralization efficiency (close to 100%), a geometric factor based on angular scattering distribution at the neutralizer surface and exit aperture of the neutralizer, and possibly others. Of course, this proportionality factor may vary with ion species due to different reflection and scattering properties upon scattering from the neutralizer surface, different secondary electron yields, and different charge-conversion efficiencies. The ion beam geometry and

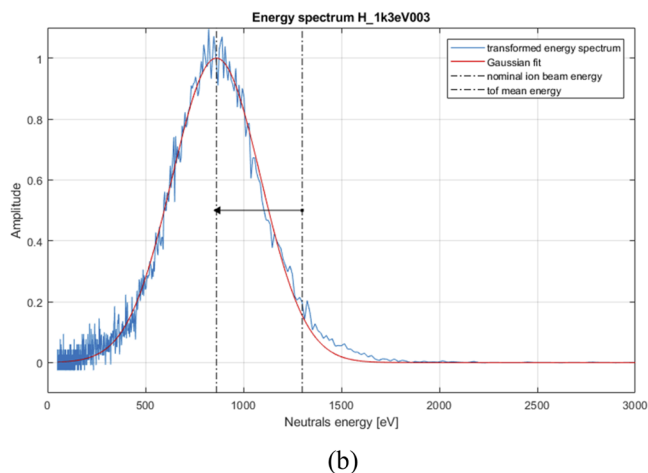
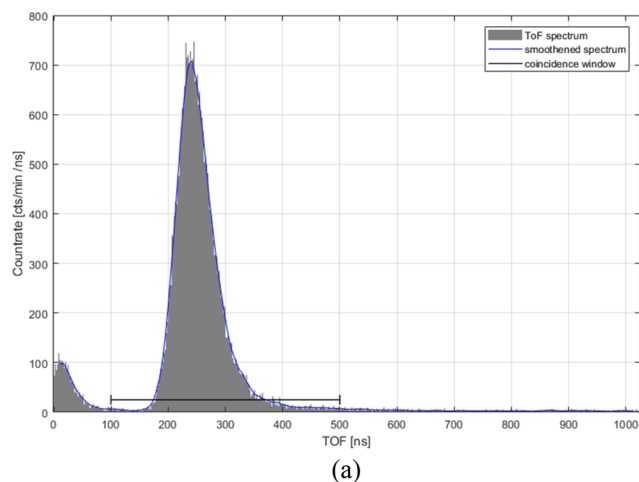


**FIG. 8.** (a) Recorded ToF spectrum from 1.3 keV hydrogen beam, with a moving average added in blue and the typical coincidence window in black. (b) The energy distribution derived from the ToF spectrum for scattered ENA beam in the ABM. Dash-dotted lines show the mean neutral beam energy (862 eV) and the primary ion beam energy (1.3 keV) as well as the mean energy loss (arrow).

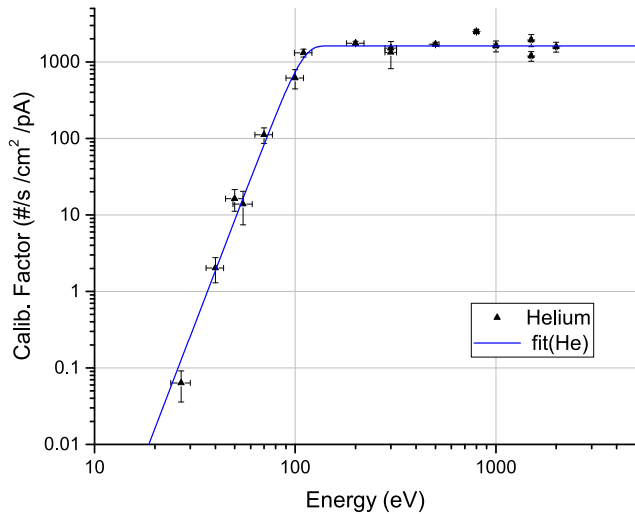


**FIG. 9.** Neutralizer calibration for helium from 3 keV down to 30 eV primary ion energy. The calibration factor is the neutral beam flux per neutralizer surface current (pA), and it is plotted as function of primary ion beam energy. Measured data are fitted with a Weibull function.

angular spread vary with ion beam energy, which, in turn, changes the neutral atom transmission through the neutralizer exit.

By relating the neutral atom flux measured by the ABM to the simultaneously measured neutralizer surface current, we obtain an absolute calibration of the surface neutralizer. For each ENA species of interest, we derive the calibration factor  $CF(E_q) = F_n/I_{ncs}$  that relates the measured current to the emitted neutral atom flux as function of the ion beam energy  $E_q$ .

One example of neutralizer calibration function is shown for He in Fig. 9. An empirical fit is added to the measured data using a three-parameter Weibull cumulative distribution function Eq. (11),

$$f(x) = a \exp(-(bx)^d), \quad (11)$$

with the parameters  $a = 1617$ ,  $b = 9.32 \times 10^{-3}$ ,  $d = 6.85$ . The Weibull function was chosen without physical meaning, but it allows good fits for a wide range of the calibration function  $f$  value at energies  $x$ . Similar neutral beam calibration measurements are prepared for IMAP for a number of species of interest, including hydrogen, deuterium, helium, and oxygen neutral atom beams down to lower beam energy limits of 10 eV (H) to 30 eV (D), for which results will be reported in a later publication.

#### IV. SUMMARY

With the absolute beam monitor, we have developed a new laboratory device that is capable of recording the neutral atom flux from an ENA beam source in the 10 eV–3 keV energy range in an absolute manner. The ABM measurement principle is based on a coincidence technique using surface scattering on a polished W surface and by recording the resulting start, stop, and coincidence signals simultaneously. In addition, the device provides a coarse measurement of the neutral atom beam energy using a simple ToF configuration.

Individual signal counts are Poisson distributed in each channel. The observed background count rates are about four orders of magnitude lower than the actual signal rates.

In the low to mid energy range, the accumulation time required to get sufficient counts can range from minutes to hours because of the low efficiencies for creating a start, stop, and coincidence signal at these low energies. Therefore, operating the ABM in parallel with a scientific ENA instrument under test is difficult. Instead, the ABM serves as an independent primary calibration standard for calibrating the beam surface neutralizer, which records a simultaneous current signal related to the neutral atom flux.

#### ACKNOWLEDGMENTS

This work was supported by the Swiss National Science Foundation.

#### AUTHOR DECLARATIONS

##### Conflict of Interest

The authors have no conflicts to disclose.

#### Author Contributions

**Jonathan Gasser:** Conceptualization (equal); Data curation (lead); Investigation (lead); Methodology (equal); Visualization (lead); Writing – original draft (lead); Writing – review & editing (equal). **André Galli:** Conceptualization (equal); Investigation (supporting); Methodology (equal); Supervision (supporting); Writing – original draft (supporting); Writing – review & editing (supporting). **Peter Wurz:** Conceptualization (equal); Funding acquisition (lead); Investigation (supporting); Methodology (equal); Project administration (lead); Resources (lead); Supervision (lead); Writing – original draft (supporting); Writing – review & editing (equal).

#### DATA AVAILABILITY

The data that support the findings of this study are available from the corresponding author upon reasonable request.

#### REFERENCES

- <sup>1</sup>P. Wurz, “Detection of energetic neutral particles,” *The Outer Heliosphere: Beyond the Planets* (Copernicus Gesellschaft e.V., Katlenburg-Lindau, Germany, 2000), pp. 251–288.
- <sup>2</sup>S. Fuselier, P. Bochsler, D. Chornay, G. Clark, G. Crew, G. Dunn, S. Ellis, T. Friedmann, H. Funsten, A. Ghielmetti, J. Googins, M. Granoff, J. Hamilton, J. Hanley, D. Heirtzler, E. Hertzberg, D. Isaac, B. King, U. Knauss, F. Kudirka, H. Kucharek, J. Lobell, S. Longworth, D. McComas, E. Möbius, A. Moore, T. Moore, R. Nemanich, P. Nolin, M. O’Neal, D. Piazza, S. Pope, P. Rosmarynowski, L. Saul, J. A. Scheer, C. Schlemm, J. Scherrer, C. Tillier, S. Turco, J. Tyler, M. Vosbury, M. Wieser, P. Wurz, and S. Zaffke, *The IBEX-Lo Sensor*, *Space Science Reviews* **146**, 117–147 (2009).
- <sup>3</sup>A. Galli, P. Wurz, S. Fuselier, D. McComas, M. Bzowski, J. M. Sokol, M. A. Kubiak, and E. Möbius, “Imaging the heliosphere using neutral atoms from solar wind energy down to 15 eV,” *Astrophys. J.* **796**, 9–27 (2014).
- <sup>4</sup>D. J. McComas, F. Allegrini, P. Bochsler, M. Bzowski, M. Collier, H. Fahr, H. Fichtner, P. Frisch, H. O. Funsten, S. A. Fuselier, G. Gloeckler, M. Gruntman, V.

- Izmodenov, P. Knappenberger, M. Lee, S. Livi, D. Mitchell, E. Möbius, T. Moore, S. Pope, D. Reisenfeld, E. Roelof, J. Scherrer, N. Schwadron, R. Tyler, M. Wieser, M. Witte, P. Wurz, and G. Zank, "IBEX — Interstellar Boundary Explorer," *Space Sci. Rev.* **146**, 11–33 (2009).
- <sup>5</sup>D. J. McComas, E. R. Christian, N. A. Schwadron, N. Fox, J. Westlake, F. Allegrini, D. N. Baker, D. Biesecker, M. Bzowski, G. Clark, C. M. S. Cohen, I. Cohen, M. A. Dayeh, R. Decker, G. A. de Nolfo, M. I. Desai, R. W. Ebert, H. A. Elliott, H. Fahr, and E. Zirnstein, "Interstellar Mapping and Acceleration Probe (IMAP): A new NASA mission," *Space Sci. Rev.* **214**, 116 (2018).
- <sup>6</sup>A. Galli, I. I. Baliukin, M. Bzowski, V. V. Izmodenov, M. Kornbleuth, H. Kucharek, E. Möbius, M. Opher, D. Reisenfeld, N. A. Schwadron, and P. Swaczyna, "The heliosphere and Local Interstellar Medium from neutral atom observations at energies below 10 keV," *Space Sci. Rev.* **218**, 31 (2022).
- <sup>7</sup>A. Galli, P. Wurz, N. A. Schwadron, K. Fairchild, D. Heitzler, E. Möbius, H. Kucharek, R. Winslow, M. Bzowski, M. A. Kubiak, I. Kowalska-Leszczynska, S. A. Fuselier, J. M. Sokol, P. Swaczyna, and D. J. McComas, "One solar cycle of heliosphere observations with the Interstellar Boundary Explorer: Energetic neutral hydrogen atoms observed with IBEX-Lo from 10 eV to 2 keV," *Astrophys. J., Suppl. Ser.* **261**(2), 18 (2022).
- <sup>8</sup>D. J. McComas, M. Bzowski, M. A. Dayeh, R. DeMajistre, H. O. Funsten, P. H. Janzen, I. Kowalska-Leszczynska, M. A. Kubiak, N. A. Schwadron, J. M. Sokol, J. R. Szalay, M. Tokumaru, and E. J. Zirnstein, "Solar cycle of imaging the global heliosphere: Interstellar Boundary Explorer (IBEX) observations from 2009–2019," *Astrophys. J., Suppl. Ser.* **248**, 26 (2020).
- <sup>9</sup>P. Swaczyna, M. A. Kubiak, M. Bzowski, J. Bower, S. A. Fuselier, A. Galli, D. Heitzler, D. J. McComas, E. Möbius, F. Rahmani, and N. A. Schwadron, "Very Local Interstellar Medium revealed by complete solar cycle of interstellar neutral helium observations with IBEX," *Astrophys. J., Suppl. Ser.* **259**, 42 (2022).
- <sup>10</sup>T. E. Moore, D. J. Chornay, M. R. Collier, F. A. Herrero, J. Johnson, M. A. Johnson, J. W. Keller, J. F. Laudadio, J. F. Lobell, K. W. Ogilvie, P. Rozmarynowski, S. A. Fuselier, A. G. Ghielmetti, E. Hertzberg, D. C. Hamilton, R. Lundgren, P. Wilson, P. Walpole, T. M. Stephen, B. L. Peko, B. van Zyl, P. Wurz, J. M. Quinn, and G. R. Wilson, "The low-energy neutral atom imager for IMAGE," *Space Sci. Rev.* **91**, 155–195 (2000).
- <sup>11</sup>S. Barabash, R. Lundin, H. Andersson, K. Brinkfeldt, A. Grigoriev, H. Gunell, M. Holmström, M. Yamauchi, K. Asamura, P. Bochsler, P. Wurz, R. Cerulli-Irelli, A. Mura, A. Milillo, M. Maggi, S. Orsini, A. J. Coates, D. R. Linder, D. O. Kataria, and J. Thocaven, "The analyzer of space plasmas and energetic atoms (ASPERA-3) for the Mars Express mission," *Space Sci. Rev.* **126**, 113–164 (2006).
- <sup>12</sup>S. Barabash, J.-A. Sauvaud, H. Gunell, H. Andersson, A. Grigoriev, K. Brinkfeldt, M. Holmström, R. Lundin, M. Yamauchi, K. Asamura, W. Baumjohann, T. L. Zhang, A. J. Coates, D. R. Linder, D. O. Kataria, C. C. Curtis, K. C. Hsieh, B. R. Sandel, A. Fedorov, and P. Bochsler, "The analyser of space plasmas and energetic atoms (ASPERA-4) for the Venus Express mission," *Planet. Space Sci.* **55**, 1772–1792 (2007).
- <sup>13</sup>S. Barabash, A. Bhardwaj, M. Wieser, R. Sridharan, T. Kurian, S. Varier, E. Vijayakumar, V. Abhirami, K. Raghavendra, S. Mohankumar, M. Dhanya, S. Thampi, K. Asamura, H. Andersson, Y. Futaana, M. Holmström, R. Lundin, J. Svensson, S. Karlsson, and P. Wurz, "Investigation of the solar wind-Moon interaction onboard Chandrayaan-1 mission with the SARA experiment," *Curr. Sci.* **96**(4), 526–532 (2009); available at <https://www.jstor.org/stable/24105464>.
- <sup>14</sup>S. Orsini, A. Di Lellis, A. Milillo, E. De Angelis, A. Mura, S. Selci, I. Dandouras, P. Cerulli-Irelli, R. Leoni, V. Mangano, S. Massetti, F. Mattioli, R. Orfei, C. Austin, J. Medale, N. Vertolli, and D. Giulio, "Low energy high angular resolution neutral atom detection by means of micro-shuttering techniques: The BepiColombo SERENA/ELENA sensor," *AIP Conf. Proc.* **1144**, 91 (2008).
- <sup>15</sup>S. Orsini, S. Livi, K. Torkar, S. Barabash, A. Milillo, P. Wurz, A. Di Lellis, E. Kallio, and SERENA Team, "SERENA: A suite of four instruments (ELENA, STROFIO, PICAM and MIPA) on board BepiColombo-MPO for particle detection in the Hermean environment," *Planet. Space Sci.* **58**, 166–181 (2008).
- <sup>16</sup>L. Kong, A. Zhang, Z. Tian, X. Zheng, W. Wang, B. Liu, P. Wurz, D. Piazza, A. Etter, B. Su, Y. An, J. Ding, W. Li, Y. Liu, L. Li, Y. Li, X. Tan, and Y. Sun, "Mars ion and neutral particle analyzer (MINPA) for Chinese Mars exploration mission (Tianwen-1): Design and ground calibration," *Earth Planet. Phys.* **4**, 1–12 (2020).
- <sup>17</sup>Y. Futaana, M. Wieser, and S. Barabash, "Low energy energetic neutral atom imaging in the Jovian system," in *2013 EGU General Assembly* (2013), no. 12291.
- <sup>18</sup>Y. Kazama, S. Barabash, M. Wieser, K. Asamura, and P. Wurz, "Development of an LENA instrument for planetary missions by numerical simulations," *Planet. Space Sci.* **55**, 1518–1529 (2007).
- <sup>19</sup>S. Barabash, P. Wurz, P. Brandt, M. Wieser, M. Holmström, Y. Futaana, G. Stenberg Wieser, H. Nilsson, A. Eriksson, M. Tulej, A. Vorburger, N. Thomas, C. Paranicas, D. Mitchell, G. Ho, B. Mauk, D. Haggerty, J. Westlake, M. Fränz, and D. Grodent, "Particle environment package (PEP)," in *Proceedings of the European Planetary Science Congress EPSC2013* (2013), Vol. 8, no. 709.
- <sup>20</sup>J. Gasser, M. Föhn, A. Galli, E. Artegiani, A. Romeo, and P. Wurz, "Cadmium telluride as a potential conversion surface," *J. Appl. Phys.* **129**, 045303 (2021).
- <sup>21</sup>J. Scheer, W. Brüning, T. Fröhlich, P. Wurz, and W. Heiland, "Scattering of small molecules from a diamond surface," *Nucl. Instrum. Methods Phys. Res., Sect. B* **157**(1), 208–213 (1999).
- <sup>22</sup>P. Wurz, R. Schletti, and M. R. Aellig, "Hydrogen and oxygen negative ion production by surface ionization using diamond surfaces," *Surf. Sci.* **373**(1), 56–66 (1997).
- <sup>23</sup>A. Marti, R. Schletti, P. Wurz, and P. Bochsler, "Calibration facility for solar wind plasma instrumentation," *Rev. Sci. Instrum.* **72**, 1354 (2001).
- <sup>24</sup>M. Wieser and P. Wurz, "Production of a 10 eV–1000 eV neutral particle beam using surface neutralization," *Meas. Sci. Technol.* **16**, 2511–2516 (2005).
- <sup>25</sup>H. O. Funsten, R. W. Harper, and D. J. McComas, "Absolute detection efficiency of space-based ion mass spectrometers and neutral atom imagers," *Rev. Sci. Instrum.* **76**, 053301 (2005).
- <sup>26</sup>M. A. Gruntman and V. A. Morozov, "H atom detection and energy analysis by use of thin foils and TOF technique," *J. Phys. E: Sci. Instrum.* **15**(12), 1356 (1982).
- <sup>27</sup>G. Betz and K. Wien, "Energy and angular distributions of sputtered particles," *Int. J. Mass Spectrom. Ion Processes* **140**(1), 1–110 (1994).
- <sup>28</sup>G. Högberg, H. Nordén, and H. Berry, "Angular distributions of ions scattered in thin carbon foils," *Nucl. Instrum. Methods* **90**, 283–288 (1970).
- <sup>29</sup>P. Wurz, J. Scheer, and M. Wieser, "Particle scattering off surfaces: Application in space science," *e-J. Surf. Sci. Nanotechnol.* **4**, 394–400 (2006).
- <sup>30</sup>W. A. de Zeeuw, H. W. van der Ven, J. M. M. de Wit, and A. J. H. Donné, "An electrostatic time-of-flight analyzer for simultaneous energy and mass determination of neutral particles," *Rev. Sci. Instrum.* **62**(1), 110–117 (1991).
- <sup>31</sup>P. Wurz, A. Balogh, V. Coffey, B. Dichter, W. Kasprzak, A. Lazarus, W. Lennartsson, and J. McFadden, "Calibration techniques," in *Calibration of particle instruments in Space Physics* (ed. M. Wüest, D.S. Evans, and R. von Steiger), ESA Communications, ISSI Scientific Report, SR-007 (2007), Chap. 3, pp. 117–276.
- <sup>32</sup>H. Niehus, W. Heiland, and E. Taglauer, "Low-energy ion scattering at surfaces," *Surf. Sci. Rep.* **17**(4–5), 213–303 (1993).
- <sup>33</sup>T. M. Stephen and B. L. Peko, "Absolute calibration of a multichannel plate detector for low energy O, O<sup>-</sup>, and O<sup>+</sup>," *Rev. Sci. Instrum.* **71**(3), 1355–1359 (2000).